

# Long-term Doppler imaging of the star XX Trianguli indicates chaotic non-periodic dynamo

Received: 6 September 2023

Accepted: 6 November 2024

Published online: 04 December 2024

K. G. Strassmeier<sup>1,2</sup>✉, Zs. Kővári<sup>3,4</sup>, M. Weber<sup>1</sup> & T. Granzer<sup>1</sup>

Sunspots are the most well-known manifestations of solar magnetic fields and exhibit a range of phenomena related to the interior dynamo. Starspots are the direct analogs of sunspots on other stars but with the big observational restriction that we usually cannot resolve other star's surfaces. In this paper we employ an indirect surface imaging technique called Doppler imaging and present 99 independent Doppler images of the star XX Trianguli. The star was selected because it had shown a gigantic star spot in a previous study and was thus well suited for a long-term monitoring effort. We combine the Doppler images into a movie visualizing the star's surface spot evolution for the past 16 years. Stellar-disk photocenter displacements of up to  $24 \mu\text{as}$ , or about 10% of the stellar disk radius, are reconstructed, but do not show the typical solar-like periodic behavior that could be interpreted as an activity cycle. It suggests a mostly chaotic, likely unperiodic, dynamo. These rotation-induced stellar photocenter variations pose an intrinsic limitation for astrometric exoplanet catches.

Among the observables from the spatially resolved solar disk are the number, size, and morphology of sunspots<sup>1</sup>, their growth and decay, and their migration in latitude and longitude. Such spots are also seen on other stars, then referred to as star spots<sup>2</sup>. We employ an indirect surface imaging technique to invert the spectral line profiles into images of the stellar surface<sup>3–8</sup>. Typically, only occasional snapshots of spots on stellar surfaces are obtainable while it is well-known that spots systematically change with time and, like on the Sun, only then tell us about the interior dynamo and structure of the target in question. We picked one of the most spotted stars in the sky (XX Trianguli) for such a more continuous application of Doppler imaging.

XX Tri (HD 12545) is a bright ( $V \approx 8$  mag) K0 giant star in a single-lined spectroscopic binary system (SBI) with a most probable mass just 10 % more massive than the Sun, a radius of  $\sim 10 R_{\odot}$ , an effective temperature of 4630 K, and a rotation period of 24 d synchronized to the orbital period of the binary (see Table 1 for a summary). The star was previously found to have a gigantic star spot<sup>9</sup> with physical dimensions  $\sim 10,000$  times the area of the largest spot group ever seen on the Sun,

equivalent to 10 times the projected solar disk. Earlier time-series Doppler imaging of a subset of the current data had revealed a linear spot decay on XX Tri of  $-0.022 \pm 0.002$  solar hemispheres per day, constraining the turbulent diffusivity in its near-surface layers and predicting a magnetic cycle of  $26 \pm 6$  years<sup>10</sup>. The star's radius still remains uncertain despite the ultra-precise *Gaia* parallax now available. The *Gaia* DR3 parallax of  $5.094 \pm 0.028 \text{ mas}$ <sup>11</sup> has refined XX Tri's distance to  $196.3 \pm 1.1 \text{ pc}$  as compared with  $160^{+32}_{-22} \text{ pc}$  from the re-reduced *Hipparcos* data<sup>12</sup> (we notice that the original *Hipparcos* parallax<sup>13</sup> converted to  $196.8 \pm 35 \text{ pc}$  and thus agreed well with the *Gaia* DR3 value despite the 30-times larger error). The NASA/IPAC dust maps<sup>14</sup> suggest a visual extinction of  $A(V) = 0.23 \text{ mag}$  in the direction of the target. The stellar radius would thus be  $8.95 \pm 0.23 R_{\odot}$ , where the error is dominated by the choice of the apparent unspotted brightness rather than the distance. At face value, this radius is smaller by about 20% compared to the radius expected from the projected equatorial rotation velocity ( $v \sin i = 20.0 \pm 0.6 \text{ km s}^{-1}$ ), the rotation period ( $P_{\text{rot}} = 24.0 \pm 0.1 \text{ d}$ ), and the inclination of the rotation axis

<sup>1</sup>Leibniz-Institute for Astrophysics Potsdam (AIP), D-14482 Potsdam, Germany. <sup>2</sup>Institute for Physics and Astronomy, University of Potsdam, D-14476 Potsdam, Germany. <sup>3</sup>Konkoly Observatory, HUN-REN Research Centre for Astronomy and Earth Sciences, H-1121 Budapest, Hungary. <sup>4</sup>HUN-REN CSFK, MTA Centre of Excellence, H-1121 Budapest, Hungary. ✉e-mail: [kstrassmeier@aip.de](mailto:kstrassmeier@aip.de)

**Table 1 | Stellar properties of XX Tri (HD 12545)**

Parameter [unit]	Value	Reference
M-K classification	K0III	9
Distance [pc]	196.3 ± 1.1	11
Maximum brightness $V_{\max}$ [mag]	7.64	this paper
Average color $V - I_C$ [mag]	1.18	19
Rotation period $P_{\text{rot}}$ [d]	24.0 ± 0.1	9 this paper
Orbital period $P_{\text{orb}}$ [d]	23.9674 ± 0.0005	10
Inclination $i$ [deg]	60 ± 10	9
Projected rotational velocity $v \sin i$ [km s <sup>-1</sup> ]	20.0 ± 0.6	this paper
Temperature $T_{\text{eff}}$ [K]	4627 ± 26	this paper
Log gravity $\log g$ [cm s <sup>-2</sup> ]	2.82 ± 0.05	this paper
Metallicity [M/H] [[Fe/H] <sub>⊙</sub> ]	-0.13 ± 0.04	10
Microturbulence $\xi_t$ [km s <sup>-1</sup> ]	1.83 ± 0.03	this paper
Macroturbulence $\zeta$ [km s <sup>-1</sup> ]	3.0	10
Radius [R <sub>⊙</sub> ]	10.95 <sup>+1.4</sup> <sub>-0.95</sub>	from $v \sin i$ , $P_{\text{rot}}$ , and $i$
	8.95 ± 0.23	from $V_{\max}$ , $T_{\text{eff}}$ , and distance
Luminosity [L <sub>⊙</sub> ]	33 ± 2	from $V_{\max}$ , $T_{\text{eff}}$ , and distance
Mass [M <sub>⊙</sub> ]	1.26 ± 0.15	10
	1.1 <sup>+0.2</sup> <sub>-0.3</sub>	this paper
Age [Gyr]	7.7 ± 3.1	10
	7.4 <sup>+2.3</sup> <sub>-3.2</sub>	this paper

Note: Stellar radius is determined either from  $R = vP_{\text{rot}}/i$  or from the Stefan-Boltzmann law based on the parameters indicated in the third column. Luminosity is determined from the Stefan-Boltzmann law with the same parameters.

( $i = 60^\circ \pm 10^\circ$ ) which are all known with high precision (even the inclination albeit not directly measured but inferred from the fits to the data; for the most recent references to these values see Table 1). Such a discrepancy had also been noted for the similar system II Peg<sup>15</sup> but also for the single star V987 Tau<sup>16</sup>. The reason is thought to be the large and ever-changing star spots of heavily spotted stars like XX Tri. Dark star spots have already been suspected to introduce astrometric jitter<sup>17,18</sup> that may render a parallax measurement imprecise or even erroneous. Dark spots repel the apparent disk photocenter from the true disk center, whereas bright faculae attract the photocenter towards them. Moreover, XX Tri's *faintest* maximum brightness within a rotational cycle recorded so far of  $V = 8.36$  mag in 1992, and the *brightest* maximum brightness of  $V = 7.76$  mag seen in 2009<sup>19</sup>, now topped by an even brighter  $V = 7.64$  mag from the Automatic Photoelectric Telescope (APT) data in 2018/19 in this paper, cannot be explained by the waxing and waning of cool star spots alone. This is because the surface cannot host more spots while the spots individually appear already very cool and dark with respect to the photosphere. It requires bright faculae in order to explain the observed brightness differences by rotational modulation<sup>9</sup> but still fails to explain the large long-term brightness change. It appears that spatially resolving the surfaces of spotted stars, and identifying their types of inhomogeneities, will help in resolving the radius puzzle for this class of targets.

In this work, we present continuous high-resolution and phase-resolved spectroscopy of XX Tri with the twin 1.2-m robotic Stellar Activity (STELLA) telescopes<sup>20–23</sup> on Tenerife for the past 16 years (2006–2022). The fiber-fed STELLA Echelle Spectrograph (SES) started operation on the STELLA-I telescope in 2006, and continued on STELLA-II since 2010 until now. The robot has observed the star on every available clear night since July 2006 (and ongoing), acquiring a

total of over 2000 high-resolution, high signal-to-noise-ratio (S/N) spectra so far. Creating this unique times series was only possible thanks to the robotic operation of the observatory. The spectrograph's white pupil design provides a resolution of  $\lambda/\Delta\lambda$  of 55,000, covering the wavelength range 390–880 nm. Additionally, differential photometry was obtained with the twin APTs Wolfgang and Amadeus<sup>24</sup> in southern Arizona for the years 1995 until the end of availability of Wolfgang in 2009 and then the retirement of Amadeus in early 2019. Here, we extend ref. 10 to 99 surface maps, which extends the time coverage from six to 16 years, a baseline even longer than a sunspot cycle. Its analysis shows a distinct non-periodic surface spot pattern that we interpret to be a signature of a non-solar chaotic dynamo.

**Results**

Spectral line profiles were recorded with STELLA between 11 and 28 times over the length of a stellar rotation (24 d), depending on weather and target visibility in the sky. It thus enabled a large number of viewing angles (phases) of the stellar surface because each line profile is a 1D representation of the visible surface in velocity space. These views are inverted into a 2D Doppler surface image approximately once per stellar rotation. The image parameter for our Doppler images is photospheric temperature as detailed in the Methods subsection Inversion parameters. For the line-profile inversion, we employ the *i*MAP<sup>25</sup> code, which is based on the combined input of many individual spectral lines per echelle spectrum, that is, per viewing phase of our target. For each of the 16 observing seasons, we obtained between 4 and 8 independent Doppler images, one per stellar rotation if weather permitted. It enabled a total of 99 independent surface images over the course of 16 years covering 237 stellar rotations (listed in Supplementary Data 1), which we then stack into a movie. A total of seven movies (Supplementary Movies 1–7) are presented.

**Resolving the stellar surface**

Figure 1 visualizes a snapshot of the main movie (Supplementary Movie 1), explaining what is being shown and featuring four surface-projection styles. It is accompanied by Supplementary Figs. 1–6 of similar snapshots of the other movies; in Mercator projection (Supplementary Movie 2, Supplementary Fig. 1), true-area Aitoff projection (Supplementary Movie 3, Supplementary Fig. 2), four-phase orthographic projection (Supplementary Movie 4, Supplementary Fig. 3), and pole-on projection (Supplementary Movie 5, Supplementary Fig. 4). Figure 2 displays a quick-look panorama of the individual Doppler images in Mercator projection. It is obvious that XX Tri underwent systematic spot emergences, decays, and also seemingly erratic rearrangements within the 16 years of its observations (the average duration of an observing season is eight months). The individual spot variability time-scale is as short as 1–2 stellar rotations (~30 d), while the large-scale spot morphology can be stable for most of the length of an observing season, say, 6–10 stellar rotations (~200 d). All images are characterized by high-latitude cool spots with a temperature difference of  $\Delta T \geq 1000$  K (defined as  $\Delta T = T_{\text{photosphere}} - T_{\text{spot}}$ ) with respect to the unspotted photosphere. The spots sometimes cover even the visible rotational pole, a region where the Sun does not show sunspots at all, but seldom appear at or near the stellar equator. XX Tri shows no (symmetric) polar cap-like spot, as seen on other active and spotted giants<sup>2</sup>, but mostly spots surrounding the polar region. The north-south hemispheric degeneracy of Doppler Imaging<sup>26</sup> is practically overcome by the large number of phases per image, the high S/N per line profile, and the intermediate inclination of the rotation axis. For a more detailed discussion, we refer to the review paper in ref. 6. Typically consisting of two spots, or spot groups, located in adjacent longitudinal hemispheres, which, at least from our data and method, confirms the earlier claim of the existence of active longitudes<sup>10</sup> and now shows its truly long-lived character. Occasionally a bright warm feature with at most  $\Delta T \approx -200$  K appears and quickly

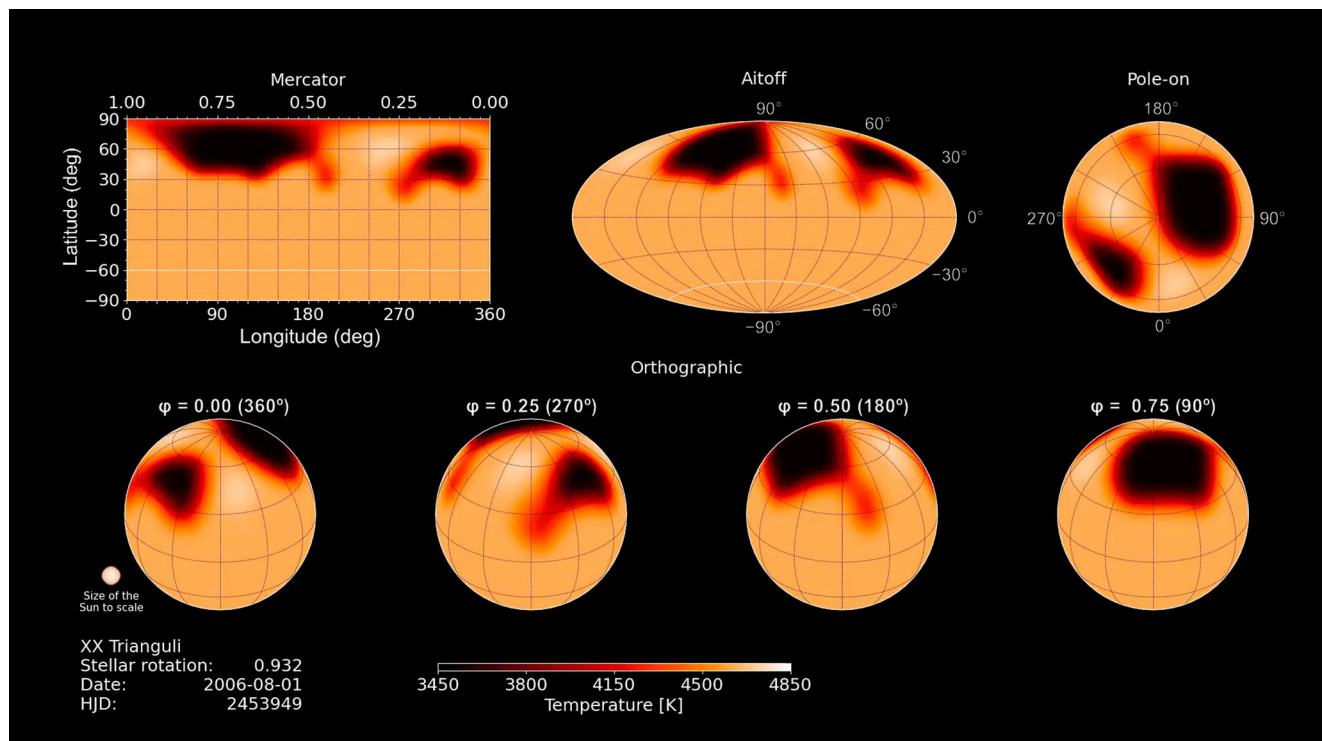


**Fig. 1 | Main movie GUI layout for the Supplementary Movies 1–7.** The main movie 1 shows four different projection styles simultaneously. In the top row, from left to right, equidistant Mercator projection, true-area Aitoff projection, and a pole-on view. The bottom row is a phase-resolved orthographic projection for four specific rotational phases ( $\phi = 0.00$ ,  $0.25$ ,  $0.50$ , and  $0.75$ ) and an inclination of  $60^\circ$ . Stellar surface longitude and latitude are always indicated in steps of  $30^\circ$ . Time is

counted in stellar rotations, in civil date, and in HJD. The real-time coverage is 237 stellar rotations from August 2006 to February 2022 (about 16 years) or 5670 days. Movie duration is three minutes and nine seconds. Surface color is always coded in terms of temperature as defined in the color bar. The four projection styles can also be viewed from individual files. Movie format is, in all cases, mp4, and all movies cover the entire 16 years of observations.

disappears again. Five such events are counted. This is also consistent with Doppler images from previous years<sup>10</sup> which had shown bright features but with a significance not always clear if real or an artifact. Our present series of surface images confirm a lower limit to the reconstructed temperatures of  $\sim 100$  K above photospheric, depending on latitude and phase coverage, which we interpret as the absolute temperature uncertainty in our data. Not a single epoch was recovered that shows XX Tri unspotted or nearly unspotted.

### XX Tri appears fainter when more spotted and brighter when less spotted

Figure 3 plots and compares the following three tracers: the stellar effective temperature from spectrum synthesis fits (panel a), the spot-filling factor (panel b) as defined in Eq. (6) in the Methods subsection Global stellar parameters, and the disk-integrated relative flux (panel c), the latter two extracted from the Doppler images. The time-averaged effective temperature is  $4627 \pm 26$  K, with an upper envelope of 4660 K and a lower envelope of 4560 K. A typical peak-to-peak amplitude due to rotation is  $\sim 50$  K. This temperature amplitude does not necessarily relate to the spot-filling factor alone. For example, starting in season 2014/15 the filling factor almost doubled by 2016.0, while the temperature amplitudes remained nearly the same during this period. On the other hand, the “warmest” effective temperatures during the 16 years were seen at the end of 2013 when the spot-filling factor and the image flux were smallest. The 16-year average spot-filling factor is 8% of the entire visible stellar surface, with a maximum of 10.2% in March 2018 (Doppler image #74, map ID 1208) and a minimum of 5.7% in September 2014 (image #49, map ID 0902). As expected, the amplitude of the rotational modulation of the disk-integrated flux scales with the spot-filling factor; typically, the lower

the filling factor, the smaller the modulation amplitude, and vice versa. Also, XX Tri appears fainter when more spotted and brighter when less spotted. Figure 3b suggests two spot-filling minima in 2015 and 2017, while a third minimum may have been reached by 2021 at the end of our time series but it remains undetermined whether the trend continued or reversed. The flux variations over the 16 years in Fig. 3c are always below  $\sim 5$ – $10\%$  of the flux relative to an immaculate disk, thus it could be interpreted as the missing flux due to cool spots. A detailed pixel-by-pixel analysis of our images will, however, be presented in a forthcoming paper.

### Disk photocenter varies with the surface star spot distribution

In this initial paper, we focus on the astrometric impact of the spot coverage of XX Tri and its causal disk-projected photocenter variability. Such intrinsic jitter from the host star could effectively jeopardize the astrometric detection of exoplanets<sup>27</sup> but, on the other hand, may enable the detection of stellar activity cycles due to cyclic photocenter offsets<sup>28</sup>. For comparison, the peak-to-peak amplitude of the solar photocenter displacement<sup>17</sup> when a large sunspot group crosses the disk would reach 0.1% of the solar radius (a radial offset of 0.001) or  $0.5 \mu\text{as}$  if the Sun were located 10 pc away from the observer and observed in the *Gaia* bandpass. Figure 4a shows our reconstruction of the image photocenter,  $x_p, y_p$ , for one stellar rotation of XX Tri, in this example for Doppler image #1. It is expressed as the offset in  $x$  and  $y$  direction as defined in Eq. (7) in the Methods subsection Doppler image photocenter in units of the projected stellar radius ( $R_\star = 1$ ). Figure 4b shows its vector sum, that is the radial offset  $r_p$  in Eq. (8), as a function of time for the entire 16 years of observation (Supplementary Movie 6, Supplementary Fig. 5). We emphasize that these photocenters are only “observed” values when computed from the observed



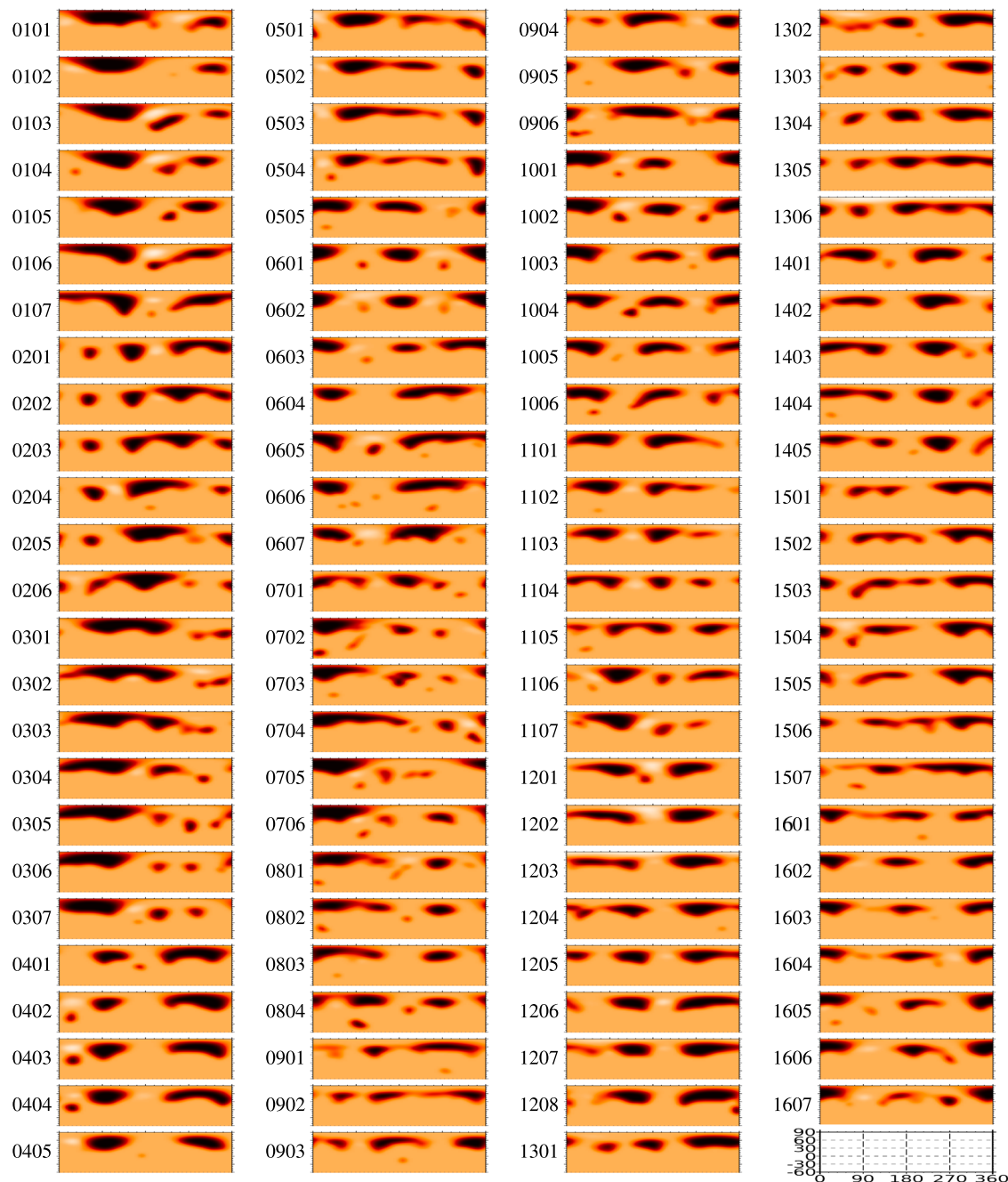


**Fig. 2 | Panorama of all individual Doppler images for 2006–2022.** Images are identified by the map ID no. from Supplementary Table 1 (first two digits are the observing season, second two digits the image number within that season). Each individual surface map is shown as a Mercator projection for the restricted latitude

range  $-60^\circ$  to  $+90^\circ$  (at an inclination of the stellar rotation axis of  $60^\circ$ ). The color coding of the temperature is the same as in Fig. 1, and in the movies. These 99 images constitute the core of the seven movies.

Doppler images (shown as blue dots in Fig. 4b), while the values from the interpolated images in the Supplementary Movie 6 for the times when the star is not visible from the ground are “predicted” values (shown as a gray line in Fig. 4b). We note that the respective movie images are in relative flux units (dubbed brightness), rather than temperature like the Doppler images, and thus represent a direct observer’s view of the stellar disk as opposed to plain temperature. Included in the temperature–flux conversion is a quadratic limb-darkening law specified for XX Tri and for the wavelengths of our spectroscopic observations. The latter is basically white light due to the large echelle format of the spectroscopic data.

#### No clean long-term cyclic changes of activity tracers

Figure 5 shows a suite of periodograms for the various surface tracers measured from the Doppler images or directly from the observed spectra (the respective time series are plotted in Figs. 3 and 4). Besides the dominant rotational modulation of about 24 days, together with its half-value and the usual aliases of about 1 year and the length of the data set, the periodograms reveal an inconclusive mixed bag of longer periods. Only the effective temperature shows significant residual power, at a period of  $1514 \pm 83$  d ( $\sim 4.1$  yr). Despite the fact that this period is likely also present in the image-integrated flux and the spot-filling factor, but with statistically insignificant levels, it is not seen in

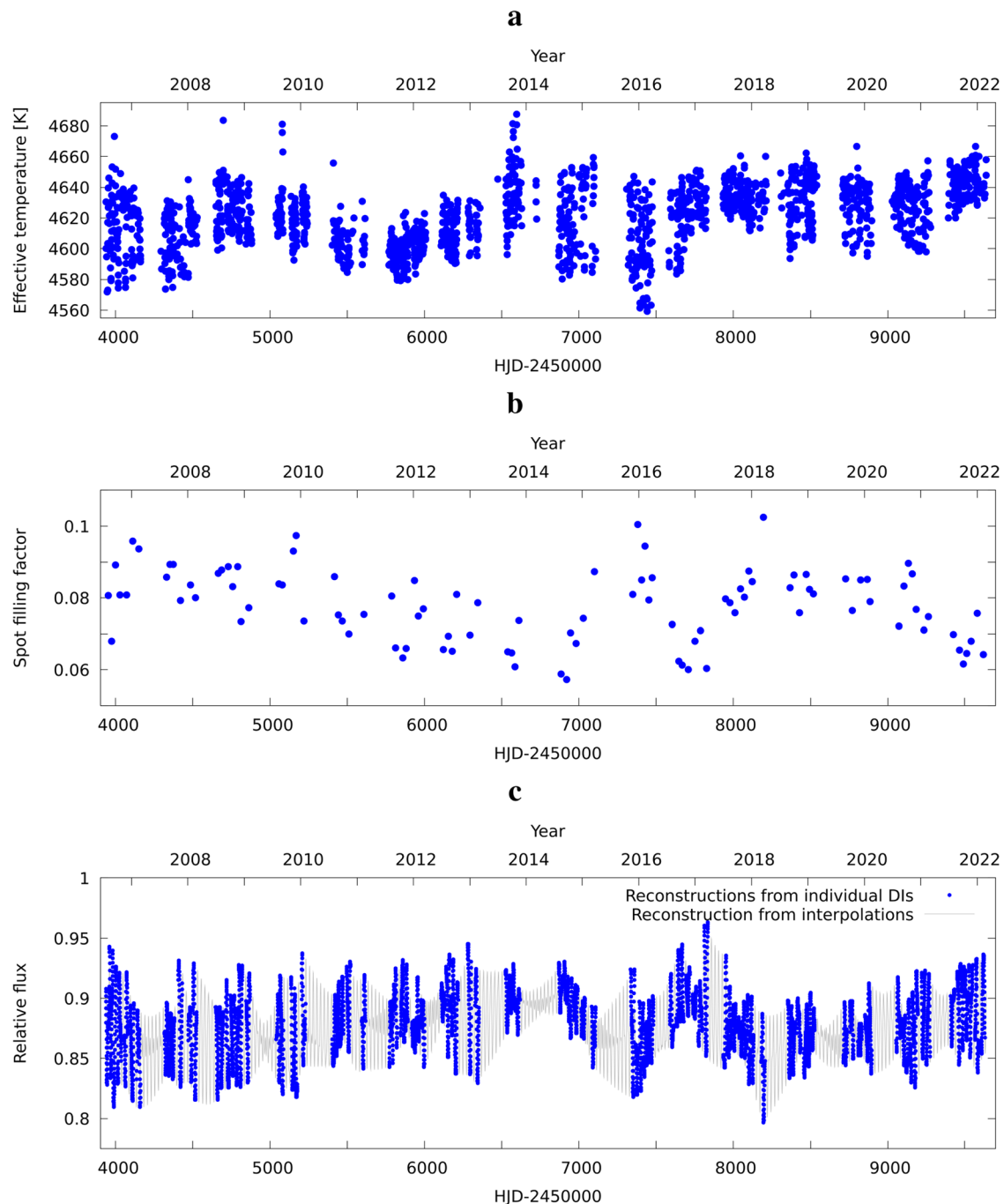


**Fig. 3 | Surface variations of XX Tri.** **a** Stellar effective temperature  $T_{\text{eff}}$  in Kelvin as obtained from a five-parameter synthetic spectrum fit to all available observations. **b** Full-time series of the spot-filling factor  $f$  as defined in Eq. (6).  $f=1$  is the entire visible stellar surface. **c** Full-time series of the relative disk-integrated flux. A relative

flux of unity is for an unspotted surface. Dots mark the reconstruction from the actual Doppler images (DIs), while the line indicates the reconstructions, including the interpolated movie images. Time is always plotted in Heliocentric Julian Days HJD. Source data are provided as a Source Data file.

the observed photocenter offsets at all. We note that the longer-period part of the periodogram of the photocenter offsets does not change when we replace the radial value with its  $x_p$  or  $y_p$  component ( $x$  in the rotation direction,  $y$  perpendicular). The shorter-period part of the periodogram does change, though, because the  $x$ -shift is more sensitive to the typical two-spot distribution on XX Tri than the  $y$ -shift and thus shows larger power at  $P_{\text{rot}}/2$  than at  $P_{\text{rot}}$ . Therefore, the photocenter offsets trace asymmetries of the surface spot distribution. We then computed the radial photocenter offsets of our Doppler images from a pole-on view (shown as an animation in Supplementary Movie 7, screenshot in Supplementary Fig. 6). That is, as if the inclination of the

stellar rotation axis would be zero degrees when the rotational modulation would be close to zero, and with the same periodogram analysis as before. As expected, there is no significant power at  $P_{\text{rot}}$  or  $P_{\text{rot}}/2$  anymore but two, equally strong, long periods at 917 d and 1660 d appear, the latter may be close to the 1514-d period from effective temperature. We note that in case we include the interpolated Doppler images (see Methods subsection Generation of the movie), these two periods slightly shift to 909 d and 1625 d, respectively, which we consider also proof that these periods are not introduced by our Doppler-image time sampling. However, the estimated errors from the widths of these period peaks are large,  $\pm 50$  d for the 900-d period and

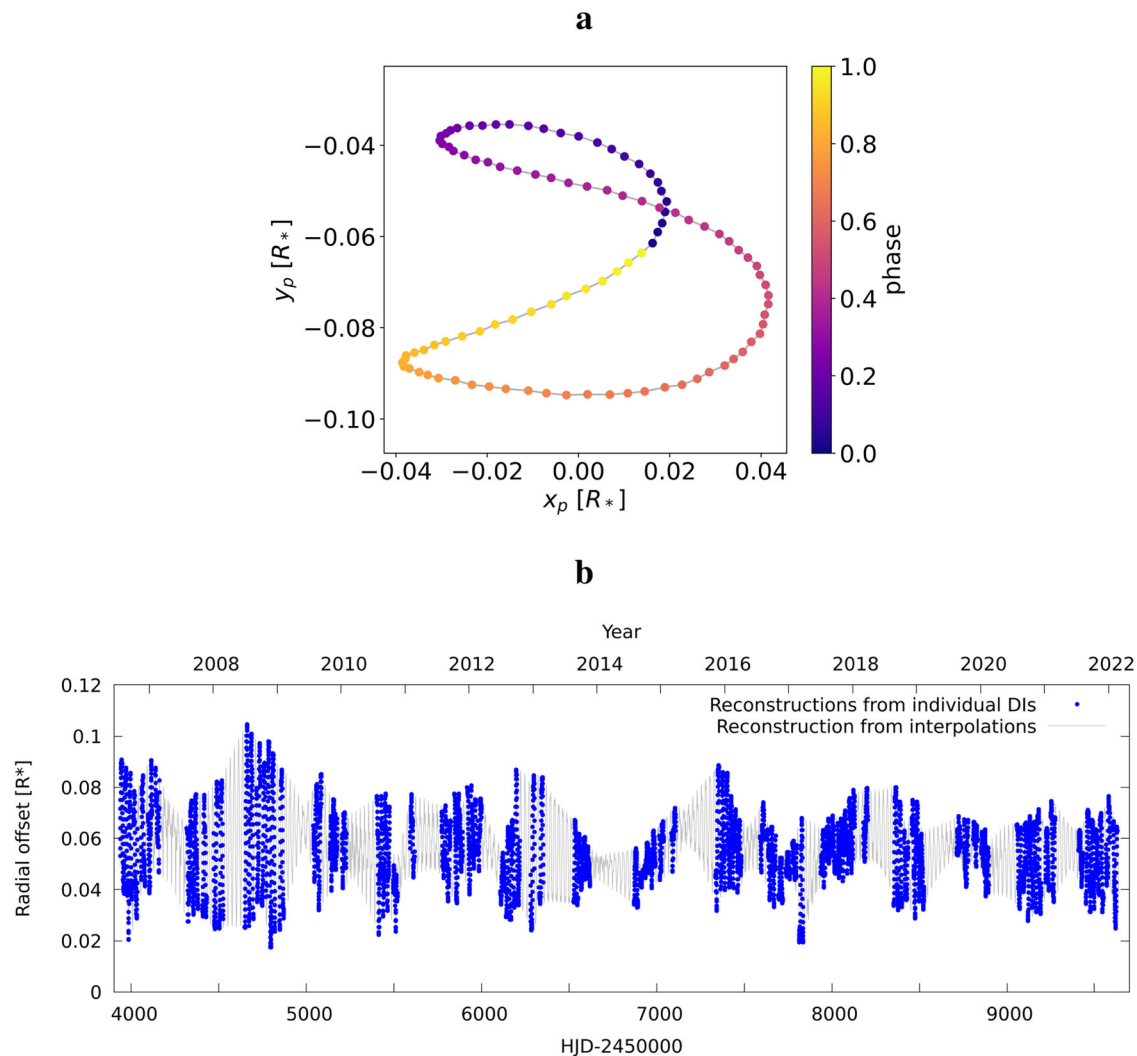


**Fig. 4 | Disk photocenter offsets for XX Tri.** **a** Displacement in units of projected stellar-disk radius during a single stellar rotation (for rotation #1 in the first observing season; see Supplementary Table 1). The color bar indicates the rotational phase. **b** Full-time series of the radial offset,  $r_p = \sqrt{x_p^2 + y_p^2}$ . Dots mark the

reconstructions from the Doppler images, the line marks the reconstructions including the interpolated movie images. The evolution of the radial offset of the photocenter over time is also available as an mp4 movie (Supplementary Movie 6). Source data are provided as a Source Data file.

even  $\pm 150$  d for the 1600-d period. This renders them uncertain in its pure existence but nevertheless strengthens the reality of the 1514-d period. Because the 1514-d period from effective temperature is the only significant period found directly, we can not readily interpret it as a magnetic or spot cycle. Therefore, we conclude that the long-term surface activity on XX Tri must be related to a more chaotic dynamo than the Sun's.

## Discussion

We recall that the solar dynamo is characterized by its twinned 22/11-yr magnetic/spot (Hale/Schwabe) cycle, recently also found for the solar twin 18 Sco<sup>29</sup>. However, a chaotic (or unperiodic) dynamo of giant-star targets similar to XX Tri had been concluded from the existence of hemispheric star spot asymmetries seen in interferometric surface images<sup>30,31</sup>. Also, a non-cyclic dynamo remains an equally likely solution from current (giant star) dynamo models<sup>32,33</sup>, given the many inherent physical assumptions even in solar dynamo models<sup>34</sup>. Because we do not know a single giant with a clear magnetic or activity cycle, nor do we have cycle predictions from model applications<sup>35</sup>, a global zero-order cycle estimate must be based on the stellar diffusion time and length scale. Such a time scale may be obtained from spot-

area decay and its inferred (magnetic) turbulent diffusivity. The length scale is typically assumed to be the depth of the convection zone, which yielded the predicted cycle for XX Tri of  $26 \pm 6$  yr<sup>10</sup>. At this point, we note, firstly, that the overlapping data with our earlier paper in ref. 10 were more consistently reduced for the present work, and, secondly, we now have an improved version of *i*MAP to our disposal. Because we still do not see clear signs of a cycle period, neither in our Doppler images nor in the broad-band photometry, it is also possible that the spot-area definition and its determination must be revised.

The observed maximum photocenter offsets for XX Tri during the 16 years amount to 10% of the projected stellar radius, or approximately  $24 \mu\text{as}$  with the *Gaia* DR3 parallax. A maximum occurred around the year 2008. The 16-year average is 6% or  $\sim 15 \mu\text{as}$ . *Hipparcos* scanned XX Tri 92-times in the years 1990–1992 and *Gaia* did it 96-times in the years 2014–2022 according to the Observation Forecast Tool at <https://gaia.esac.esa.int/gost/>. Only the *Gaia* observations are within our Doppler imaging period. However, they missed the epoch of the largest displacement in 2008. With respect to the quoted DR3 parallax error of  $28 \mu\text{as}$ <sup>11</sup>, the observed photocenter displacements are formally always below this error but clearly are non-negligible. Therefore, the *Gaia* DR3 parallax error of XX Tri, in reality, is likely

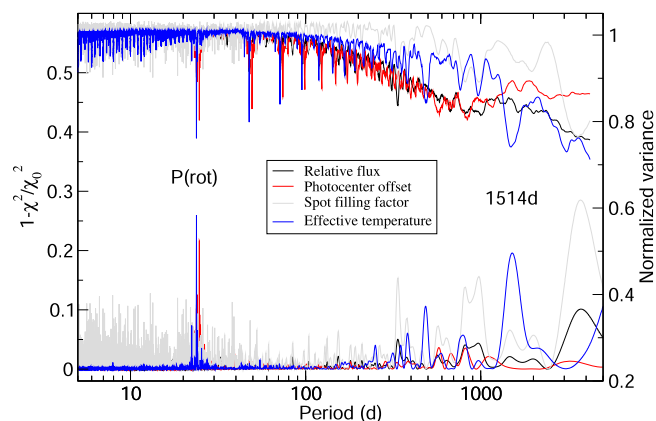


**Fig. 5 | Periodograms of four spot tracers on XX Tri.** The top set of lines is from a phase dispersion minimization given in units of its normalized variance (right axis); the bottom set of lines is from the generalized Lomb-Scargle approach given in units of  $1 - \chi^2/\chi_0^2$  (left axis). The color of the lines indicates the tracer: disk-integrated relative flux (black; data shown in Fig. 3c), photocenter offset (red; data shown in Fig. 4b), spot-filling factor (gray; data shown in Fig. 3b), and effective temperature (blue; data shown in Fig. 3a). Indicated are the rotation period  $P(\text{rot})$  at 24 d and the only significant long period at 1514 d from the effective temperature. Source data are provided as a Source Data file.

significantly larger. The independent comparison with the photometry (Supplementary Fig. 12) confirms that Doppler images are essentially capable of recovering the photometric amplitudes. All this suggests that the temperature and size of the spots shown at different phases and times in this paper are real, that is, the displacement of the photocenter also being a reliable parameter.

Stellar photocenter drifts with time already had been on the concern list for the reference-frame tracking of NASA's *Gravity Probe B* satellite. Its astrometric error budget<sup>36</sup> included the impact of a spotted stellar disk of the satellite's guide star IM Peg, a well-known magnetically active and spotted RS CVn binary, just like XX Tri. These authors referred to contemporaneous time-series Doppler imaging<sup>37–39</sup> in quoting an astrometric error of no more than  $0.04 \text{ mas yr}^{-1}$  due to spots. In the same paper<sup>36</sup> it was concluded that the combined (astrometric) error from dark spots, neighboring stars, a surrounding nebula, and the photometric variability of IM Peg, was in total smaller than  $0.05 \text{ mas yr}^{-1}$ . However, there was no analysis for spot-related optical displacements of IM Peg's projected disk in either of the above references. In this respect, our values for XX Tri are the first ever such measures of a stellar photocenter. Nevertheless, these measurements support the basic conclusions for the astrometric error budget of IM Peg, albeit its overall amplitude is more than a factor two smaller than the one suggested for IM Peg. XX Tri's maximum  $24 \mu\text{as}$  modulation with the stellar rotation period (24 d) is certainly a large value for spotted stars but similar to the expected astrometric displacement from a Saturn-mass planet in a one-year orbit around a Sun at about 100 pc. However, it is many times higher than the displacement for shorter-period exoplanets. Early planet-catch simulations<sup>40</sup> for *Gaia* had nicely demonstrated that short-period systems ( $\leq 40 \text{ d}$ ) have expected astrometric signatures of typically below  $1 \mu\text{as}$  (with a full range between  $0.01$  to  $-10 \mu\text{as}$ ). These authors predicted a planet catch of tens of thousands of systems for the nominal *Gaia* mission lifetime. Given our spot-induced photocenter offsets for XX Tri it appears very challenging to separate these two effects, rotationally modulated spots and exoplanets, in particular if of similar periodicity.

After removing the persistent (average) photocenter displacement of XX Tri from its *Gaia* DR3 parallax, we find a stellar radius of  $8.98 \pm 0.23 R_{\odot}$  instead of  $8.95$ . This small a difference appears insignificant given the error contribution from the other parameters, in

particular from the apparent brightness. It does not by far explain the previously mentioned 20% difference between the parallax-based radius to the  $v \sin i$ ,  $P_{\text{rot}}$ , and  $i$  based radius. It is more likely that we must rethink the concept of unspotted brightness in the presence of strong global stellar magnetic activity. The observed maximum brightness used in conjunction with the parallax may not be the brightness that the star would have if there were no spots. Even the currently brightest observed level of XX Tri ( $V=7.64 \text{ mag}$ ) likely underestimates the true unspotted brightness significantly. We suspect that the continuously blocked flux by these large cool spots is redistributed on a global scale rather than locally through an increase of, for example, faculae activity. It thereby alters the effective temperature and the brightness of the star on a time scale likely much longer than the stellar rotation. This view is supported by our Doppler imagery which shows that warm surface features, like faculae, are small and rare on XX Tri and thus do not significantly contribute to the  $V$ -band brightness. With an estimated missing flux for XX Tri of 10% from Fig. 3c at the time of maximum brightness near 2019.0, we would expect an unspotted  $V$  brightness about 0.1 mag brighter than even the brightest observed state so far, which would then bring the parallax-based radius close to the error range of the rotation-based radius.

## Methods

### Data description

Supplementary Data 2 is the observing log from STELLA/SES and lists all spectra used in this paper (full table only electronically). Supplementary Fig. 7a shows a 70-Å excerpt of an example SES spectrum of XX Tri from 2021, while Supplementary Fig. 7b visualizes the time and phase sampling of all approximately 2000 STELLA spectra in terms of RV. A Lomb-Scargle period fit to all STELLA RVs gives a period of  $23.9680 \pm 0.0008 \text{ d}$ , in excellent agreement with the previously determined orbital period. Its residuals are also shown in the lower left panel of Supplementary Fig. 7b. The phase-folded RV data are plotted in the right panels along with its residuals. These orbital RV residuals show the rotational modulation signal from the star spots. It is apparent that XX Tri exhibits residual RV variations due to spots between 2 and  $4 \text{ km s}^{-1}$  on an annual basis.

We adopted an integration time of 7200 s per spectrum. The S/N increased significantly over the years but shows the usual variations due to changing weather conditions and air mass. The increase was due to the combined effects of an image slicer, new fibers with better throughput, ever-better optical alignment, and the focus switch from STELLA-I to STELLA-II. Until 2013 (JD 2,456,400), the average S/N was 120 per pixel but thereafter increased to 330 with lows of  $\sim 50$  and highs of above 500. We emphasize that all data were newly and consistently reduced, which included the earlier data in ref. 10. The better S/N also allowed for a less restrictive phase sampling compared to 2015 paper<sup>10</sup> and, for a few occasions, the use of low-S/N spectra that were excluded in the earlier analysis. This is why the division of the datasets for the individual stellar rotations is not exactly identical then and now.

RVs were extracted automatically by our data-reduction pipeline. It cross-correlates 60 of the 80 echelle orders with a pre-defined and stored synthetic spectrum for a temperature of 5000 K and  $\log g$  of 2.5. Typical RV precisions of  $\sim 100 \text{ m s}^{-1}$  per observation were obtained, limited by the rotational line broadening and dependent on the actual S/N. However, the seasonal average root-mean-square (RMS) over the 16 years was comparable.

Supplementary Fig. 8 shows the APT  $V$ -band photometry for the years 1996–2019. All measures were made differentially with respect to HD 12478 ( $V=7.710 \text{ mag}$ ) as the comparison star and SAO 55178 as the check star. Three measures were usually taken per night. One observation consisted of three 10-s integrations on the Variable, four integrations on the Comparison star, two integrations on the Check star, and two integrations on the Sky. On Amadeus (=T7), the standard error of a nightly mean from the overall seasonal mean was  $0.004 \text{ mag}$  in



Johnson-V until 2012 but deteriorated thereafter to 0.015 mag in 2019. On Wolfgang (=T6), the standard error of a nightly mean was 0.003 mag in Strömgren- $y$ . Data until 2013 were published and described earlier<sup>9,19</sup>, but data between 2014–2019 had been unpublished.

### Doppler imaging: method

Doppler imaging<sup>3–8</sup> is a computational technique, similar to medical tomography, that inverts a series of high-resolution spectral line profiles into an image, in our case, of the stellar surface. Cool starspots produce pseudo-emission bumps in an absorption line profile that move from blue to red across the line as the spots rotate across the visible hemisphere due to stellar rotation. The relative velocity of migration reveals the feature's latitude. The velocity range in the line profile is restricted by the Doppler effect of the rotating stellar surface, while the intensity range is given by the temperature contrast between the spotted and unspotted photosphere. It is the way in which these distortions are modulated over a rotation period that allows the reconstruction of the stellar surface.

Most Doppler-imaging codes<sup>26,41–44</sup> use regularized inversion techniques, such as the maximum-entropy method, to determine the simplest possible image of the stellar surface that produces a statistically acceptable fit to the observed temporal sequence of line-profile distortions. An essential part of the iterative inversion process used to recover the image is that an error function is made up, which contains the sum of the squared differences between the computed line profile,  $R_{\text{comp}}$ , and the observations,  $R_{\text{obs}}$ , where  $R_{\text{obs}}$  represents the actual observed line profiles of the star per wavelength bin,  $\lambda$ , at various phases,  $\phi$ , of its rotation. This error, or discrepancy, function  $D$  in Eq. (1) is

$$D_{\lambda}(\phi) = \frac{1}{n_{\phi} n_{\lambda}} \sum_{\phi=1}^{n_{\phi}} \sum_{\lambda=1}^{n_{\lambda}} g(\phi, \lambda) [R_{\text{obs}}(\phi, \lambda) - R_{\text{comp}}(\phi, \lambda)]^2 \leq \sigma^2 \quad (1)$$

with  $n_{\phi} n_{\lambda}$  being the available numbers of phases and pixels per line profile, respectively, and  $\sigma$  the observational uncertainty and  $g(\phi, \lambda)$  a weighting function usually adopted as the inverse S/N per pixel. Typically a technique such as conjugate gradients is used for the minimization. The computed line profile  $R$  is commonly written in Eq. (2) as

$$R_{\text{comp}}(\phi, \lambda) = \frac{\iint I_c[M, X(M)] R_{\text{loc}}[M, X(M), \lambda_0 + \Delta\lambda_D(M, \phi)] \cos \theta \, dM}{\iint I_c[M, X(M)] \cos \theta \, dM}, \quad (2)$$

with  $dM = dx \, dy$  an areal surface pixel,  $I_c$  the continuum intensity,  $R_{\text{loc}}$  the local line profile,  $\Delta\lambda_D$  the Doppler shift,  $\cos \theta$  the fore-shortening angle, and  $X(M)$  the unknown image reconstruction parameter, in our case surface temperature.

Because the above problem is ill-posed, one introduces a regularizing functional,  $r$ , that helps to select the best solution (image); Eq. (3) writes it as

$$D[X(M)] + r[X(M)] = \text{minimum}. \quad (3)$$

It acts like a penalty function whose role is to increase  $D$  if detail appears in the map that exceeds the minimum necessary to fit the data to the level of the inverse S/N. If the data are of very good S/N, the choice of  $r$  is of little or no significance because external errors usually predominate. In the present approach, we use an iteratively regularized Landweber method<sup>45</sup>. The Landweber iteration realizes a simple fixed-point iteration derived from minimizing the sum of the squared errors. Its semi-convergence requires a stopping rule before it enters the noise level of the data, which is fixed by an upper bound for the data error.

### Inversion parameters

The stellar surface of XX Tri in this paper is reconstructed using the *i*MAP code<sup>25,46</sup>. The code can either perform multi-line inversions for a large number of photospheric line profiles simultaneously or use a single average line profile. For the present application, we created an average from 40 spectral lines with line depths larger than 40% of the continuum. Weaker lines were excluded because they usually decrease rather than increase the S/N of the average profile. These 40 lines were hand-selected for the spectrum of XX Tri in the sense of minimizing blending<sup>10</sup>. We input this line list with atomic data from the Vienna Atomic Line Database VALD-3<sup>47</sup>. The averaging relies on a Singular-Value-Decomposition (SVD) algorithm and a bootstrap-permutation test to determine the dimension (rank) of the signal subspace. The eigenprofiles of the signal subspace are then cross-correlated with the candidate lines to reconstruct a mean profile. The noise estimate for the SVD reconstructed data can be directly obtained from the error estimates provided by the bootstrap procedure. The weighted mean profiles have typical S/N of 1000–2000 per pixel compared to 200–300 per pixel for an individual line. We recall that the line profiles in our earlier paper<sup>10</sup> were built with a denoising approach in the wavelength domain based on a line-by-line wavelet transform (but of the same 40 spectral lines as in the present paper). The standard deviation of the individual wavelet scales (which included a 3- $\sigma$  clipping) then described the data error.

In *i*MAP's iterative inversion approach, the step size and an appropriate stopping rule provide the regularization of the inverse problem. The stopping rule assumes a number of fixed iterations derived from minimizing the sum of the squared errors per iteration (minimizing the discrepancy integral in Eq. (3)). Typically, several hundred iterations are performed per image.

For the local line profile computation, *i*MAP solves the radiative transfer per surface pixel  $dM$  and for 72 depth points with the help of an artificial neural network. Opposite to the global spectrum synthesis, *i*MAP uses a grid of tabulated Kurucz ATLAS-9<sup>48,49</sup> model atmospheres to compute line profiles in 1D and in local thermodynamic equilibrium (LTE). The grid covers temperatures between 3500 and 8000 K in steps of 250 K interpolated to the gravity, metallicity, and micro-turbulence from the global synthesis fits. The stellar surface is thereby partitioned into  $5^\circ \times 5^\circ$  segments ( $72 \times 36$  pixels), resulting in a total of 2592 surface segments for the entire sphere. Because of the inclination of  $60^\circ$ , a total of 432 segments remain always hidden, and therefore, only 2160 segments are included during the inversion process.

### General assumptions

The most vulnerable astrophysical parameter to be known and fixed prior to the inversion is the rotation period of the star. The fact that XX Tri is a binary with its visible component's orbital and rotational motion synchronized, provides us with the opportunity to adopt the much more precise orbital period as the long-term average of the surface rotation period. This places our rotational phases into a more accurate time frame along the 16-year coverage than a typically 100-times less precise photometric measurement of the rotational period would allow. Rotational epochs and phases,  $E, \phi$ , for XX Tri are thus computed from the time of observation ( $HJD$ ) via Eq. (4) as

$$HJD = 2,453,926.6663 + 23.9674 \times E \cdot \phi. \quad (4)$$

where 23.9674 d is the orbital period of the binary<sup>10</sup>. The implicit assumption in this case is that we relate surface longitudinal spot motions always to the co-rotational latitude. For a differentially rotating surface, like for XX Tri and likely all cool stars, this is the latitude where  $P_{\text{rot}} = P_{\text{orb}}$ . We emphasize that differential surface rotation does not need to be a free parameter in the present inversion procedure because our observational phase coverage is complete within mostly a single stellar rotation and thus would not contain a



signal from a differentially rotating surface. Instead, differential rotation can be inferred from a posteriori image-to-image comparison. We also note that an implicit assumption (with all Doppler images of any star) is that the time resolution can not be better than one stellar rotation because one uses information from many different phases to constrain the entire image. Intrinsic spot changes during one rotation will be smeared out and time-averaged during the reconstruction.

Standard assumptions are made in the computation of the immaculate line profiles, that is, the line profiles without the surface inhomogeneities that one wants to reconstruct. Our procedure is based on spectrum synthesis with model atmospheres and 1-D radiative transfer in LTE. We mask (exclude) spectral regions from the synthesis that are known to be prone to chromospheric magnetic activity. Besides resonance lines with extended wings, the mask also excludes strong and saturated lines with likely non-LTE contributions in their core. The resulting fits from the spectrum synthesis for global effective temperature, gravity, metallicity, and turbulence are then the values that determine the immaculate line profiles, which, in turn, are used as starting values for the line-profile inversion.

The above effective temperature and metallicity are combined with the DR3 parallax and then define our most probable mass and age of XX Tri from fits evolutionary tracks and isochrones. Employed is our minimization code APOFIS<sup>50</sup> with the newest generation of isochrones based on PARSEC<sup>51</sup>. We proceed the same way as described in ref. 50 and obtain a most probable mass for XX Tri of just 10% higher than the Sun's and an age of 7.4 Gyr. Its error bars are from the propagated measurement errors only (no isochrone errors) and are listed in Table 1.

We assume a spherical stellar surface for XX Tri. Because the ellipticity effect had been claimed to be of significant impact for the interpretation of photometric, astrometric, and spectroscopic maps of binary components<sup>52,53</sup>, we also compute a Roche-lobe model for XX Tri (using Nightfall<sup>54</sup>) based on the known binary orbit<sup>10</sup>. Its critical equipotential surfaces represent the stellar surfaces of the two binary stars. This gives the formally expected stellar radii in all directions for predetermined masses and plain Roche-lobe geometry. Comparable maximum and minimum radii for the primary ( $R_{\max}$ ,  $R_{\min}$ ) are then obtained by fitting an ellipsoid to the Roche geometry by using the forward PHOEBE<sup>55</sup> software. Due to XX Tri being a SB1 system with only a mass function known rather than individual masses, we must assume the individual masses. We chose three mass combinations ( $M_1$  mass primary,  $M_2$  mass secondary; in solar units) that fit the mass function to within its errors: (1) Minimal masses ( $M_1 = 0.8$ ,  $M_2 = 0.258$ ), which lead to  $R_{\max} = 1.0087$  and  $R_{\min} = 0.9956$  in relative units. (2) Most probable masses ( $M_1 = 1.1$ ,  $M_2 = 0.314$ ):  $R_{\max} = 1.0059$ ,  $R_{\min} = 0.9970$ , and (3) Maximal masses ( $M_1 = 1.3$ ,  $M_2 = 0.348$ ):  $R_{\max} = 1.0048$ ,  $R_{\min} = 0.9976$ . Therefore, the ellipticity as defined by  $\varepsilon^2 = 1 - (R_{\min}/R_{\max})^2$  is  $\varepsilon = 0.13^{+0.09}_{-0.06}$ , that is, less than half the value for the RS CVn binary  $\zeta$  And ( $\varepsilon = 0.27$ )<sup>52</sup> and still much smaller than for  $\sigma$  Gem ( $\varepsilon = 0.20$ )<sup>53</sup>. Note that the largest ellipticity is predicted for the minimal masses, which is the least likely version for XX Tri<sup>10</sup>. The Roche-volume filling is at 49% with a predicted full light-curve amplitude of 8 mmag for the most probable masses, compared to 81% and 70 mmag for  $\zeta$  And<sup>52</sup>, and 61% and 20 mmag for  $\sigma$  Gem<sup>53</sup>. From this, we conclude that the elliptic shape of XX Tri is negligible for our Doppler imaging.

Test inversions were carried out in order to constrain the inclination of the stellar rotational axis prior to the full-time-series application. The inclination range found was basically identical to the one in the earlier study in ref. 9 from 1999 but was less well defined. We believe that this is because in 1999, we caught the star during a light-curve variability maximum at a record amplitude of 0.63 mag in V. The accompanying line profiles changed markedly when changing the inclination and constrained the inclination to within  $\pm 10^\circ$ . The current long-term photometry shows that the star had not returned back to a similar extreme state during the time of our Doppler imaging in this paper. Our imagery reconstructs a spot distribution more-or-less

confined to high latitudes for these 16 years. This means that the line profiles are not so sensitive to the inclination due to the restricted range of occupied spot latitudes on the surface. Our  $\chi^2$  fit quality versus inclination remains basically unchanged for the  $50\text{--}70^\circ$  range with only minor differences (for  $i = 70^\circ$ :  $\chi^2 = 0.00612$ ,  $i = 65^\circ$ : 0.00601,  $i = 60^\circ$ : 0.00594,  $i = 55^\circ$ : 0.00585,  $i = 50^\circ$ : 0.00589). However, if we assume the stellar rotational axis perpendicular to the orbital plane, we may use the observed RV curve for an independent (orbital) inclination test. It gives a most likely orbital inclination of  $63^{+5}_{-2}$  (assuming the most probable stellar masses), in good agreement with our rotation-axis inclination from Doppler imaging. We conclude that the original 60-degree value from ref. 9 appears to remain the most reasonable choice which we keep fixed for the entire time series.

### Global stellar parameters

Spot coverage in this paper is given in terms of spot-filling factor  $f$  in Eq. (5) based on the common definition

$$T_{\text{eff}}^4 = f T_{\text{spot}}^4 + (1 - f) T_{\text{phot}}^4, \quad (5)$$

with  $T_{\text{eff}}$  the effective temperature,  $T_{\text{spot}}$  the spot temperature, and  $T_{\text{phot}}$  the photospheric temperature. Because our line-profile inversion is not limited to a single-valued spot temperature, we instead compute  $f$  in Eq. (6) with any temperature from all visible surface pixels. It is then a weight for how many of the visible surface pixels had to be altered in order to fit the line profiles:

$$f = 1 - \sum_{i=1}^n \cos \beta_i T_i^4 / \left( T_{\text{eff}}^4 \sum_{i=1}^n \cos \beta_i \right), \quad (6)$$

where  $\beta_i$  is the latitude of the  $i$ th pixel and the sum covers the  $n = 2160$  pixels of the part of the stellar surface above  $-60^\circ$  latitude;  $f = 1$  means the entire visible stellar surface is spotted,  $f = 0$  defines the immaculate surface.

Detailed stellar parameters were obtained with the multi-parameter minimization code ParSES<sup>56</sup> based on MARCS<sup>57</sup> model atmospheres. ParSES utilizes a grid of pre-computed template spectra built with Turbospectrum<sup>58</sup>. Its best-fit parameter search is based on the Minimum Distance Method with a non-linear simplex optimization<sup>59</sup>. For the spectrum synthesis, we adopted the original *Gaia*-ESO clean line list<sup>60</sup> with various mask widths around the line cores between  $\pm 0.05 \text{ \AA}$  to  $\pm 0.25 \text{ \AA}$ . The comparison is done spectrum by spectrum for the selected wavelength range. Like for the RVs, a selection mask identifies and removes wavelength regions from the minimization at the echelle order edges, of strong telluric contamination, and of spectral resonance lines with broad wings like  $H\alpha$ ,  $H\beta$ , or the Na D lines. The number of free parameters in the initial application of ParSES was five (effective temperature  $T_{\text{eff}}$ , gravity  $\log g$ , metallicity [M/H], projected rotational velocity  $v \sin i$ , and micro-turbulence  $\xi_t$ ). Because the synthesis fit is affected by the line-profile deformations from surface spots, it results in synthesized stellar parameters that are rotationally modulated. While this is intrinsically expected for the surface parameter  $T_{\text{eff}}$  (or stellar brightness), and nicely seen in the light curve in Supplementary Fig. 8, it is not physical for the other stellar parameters like, for example, gravity but is due to the unavoidable five-parameter fitting cross talk. Therefore, we fixed the stellar parameters other than temperature to the long-term averaged values, and then re-synthesized the spectra with only  $T_{\text{eff}}$  as a free parameter. Figure 3a shows the result for the entire spectral data set of XX Tri. The time-averaged values of the other four parameters and their RMS are given in Table 1.

### Phase-gap filling

Observational phase gaps are usually due to bad weather. In our time series they range between 1–5 d or 0.04–0.21 stellar rotations, with

maximum gaps of about 0.20 rotations occurring 31 times during the 16 years. In order to minimize spurious surface features during the line-profile inversion due to such phase gaps, we apply a phase-gap filling procedure<sup>10</sup> prior to inversion. This ensures that maps with intrinsically different phase coverage are directly comparable over time. The procedure is simply filling an existing phase gap with an observation from one rotation earlier or later, if available, and whichever has better S/N but never using a spectrum twice. This is a simple method that minimizes the systematics, even if the spots may have slightly evolved during the time covered. Simulations<sup>10</sup> with artificial phase gaps and different phase distributions proved its superiority compared to image reconstructions with unfilled gaps.

Supplementary Fig. 9 is an example of the typical annual phase coverage. It also shows the typical phase gaps for individual Doppler images. For the example of season 2021/2022, a gap of 0.17 phases occurred only for two of the seven images. The others remained with gaps well below 0.15 phases.

### Individual maps: fit quality and example result

The fit quality is judged on the minimum sum of the squared residuals, commonly written as observed minus computed (O-C) values, derived for all pixels in all line profiles per data set. Each image is treated thereby fully independently. The stopping rule in the Landweber inversion avoids line-profile over fitting by regularizing the fit procedure before it enters into the noise level of the data. The data noise itself is given for each of the SVD reconstructed line profiles from the initial bootstrap procedure (see Methods subsection Inversion parameters) and is basically equal to the error per pixel (velocity bin), that is, the inverse S/N. Because our datasets have comparable S/N over the 16 years, albeit less at the start of observations and more at the end, the fit quality per image is approximately always the same. An example of the fit quality is shown in Supplementary Fig. 10 for the seven datasets of observing season 2021/22. Supplementary Fig. 11 shows the corresponding seven temperature maps for this example result. It enables a detailed (visual) tracking of surface features from one stellar rotation to the next.

At this point, we also note that phase smearing due to the 2 hours integration time per line profile amounts to 0.0035 rotational phases, or approximately one degree at the stellar central meridian, and is thus negligible. With the current resolving power of  $\lambda/\Delta\lambda$  of 55,000 (i.e., approximately 0.10 Å at an average wavelength) and a full width of the lines at continuum level of  $2(\lambda/c)v\sin i \approx 0.8$  Å, we have eight resolution elements across the stellar disk.

A comparison of the predicted brightness variations from our Doppler images with the V-band APT photometry is shown in Supplementary Fig. 12. As emphasized in the main text, the observed long-term brightness trend is not explained with our (purely photospheric) Doppler images, and we must remove the observed long-term V-band trend from the APT data prior to a direct comparison. Therefore, we de-trended the APT data by normalizing the seasonal average brightness such that the average is at  $\Delta V = 0$  in Supplementary Fig. 12. Because our time coverage is 16 years and this de-trending likely imperfect, we still see residual season-to-season changes that are non-periodic and due to a residual, possibly chaotic, long-term trend. Nevertheless, the predicted light curves from the Doppler images match the photometric rotational modulation reasonably well. This reassures that the temperature and extent of the spots are real and not just a numerical artifact.

Our maps reconstruct five warm surface features within 16 years. These features are required by the data and are usually seen over more than a single stellar rotation. We had shown in the past that warm features can be consistently reconstructed in simulations<sup>61</sup>, at least at the  $2-3\sigma$  level (one sigma  $\sim 50-70$  K), but also from real data<sup>62</sup> of stars with known hot features (of up to 2000 K above photospheric). The fact that we employ a full radiative transfer solution to obtain each surface pixel's temperature assures that we get the relative specific

intensity right. At this point, we emphasize that the 40 hand-selected spectral lines are part of the strategy to fight artifacts. These 40 lines' atomic parameters are very well determined and make sure that we do not have, for example, line saturation effects at the edge of the expected range of surface temperatures. The reconstructions show the warm features five times smaller and 150-K cooler than what was reconstructed from the line profiles in 1998<sup>9</sup> during an epoch of extreme light-curve amplitude (0.63 mag). No such extreme light-curve amplitudes were observed thereafter and our Doppler images accordingly also did not predict such. It is thus unlikely that these features are the sole cause for the long-term brightness increase.

### Doppler image photocenter

We define the image photocenter as the point on the apparent disk from which the light would come if the entire (spotted) disk were replaced by a single point. Therefore, it is calculated as a kind of "center of gravity" of the limb darkened intensity map of the apparent disk. For the computation, every (visible) surface pixel temperature  $T_i$  is converted to a relative surface flux via a simple black-body assumption ( $F \propto \lambda, T$ ) together with the appropriate fore-shortening angle. We included a quadratic limb-darkening law specified for the wavelength range of our line profiles (4500–6500 Å). The limb-darkening coefficients for the stellar parameters of XX Tri were obtained from the web application of the JWST Exoplanet Characterization Toolkit (ExoCTK)<sup>63</sup>, based on batman<sup>64</sup> and ATLAS-9<sup>48</sup> model atmospheres. The retrieved coefficients were 0.745 for the linear term and 0.039 for the quadratic term.

The image of the relative flux distribution in orthogonal projection (with an inclination of the rotational axis of 60°), at any given time or phase, is then used to find the intensity maximum in an  $x|y$  coordinate system with the positive  $x$  axis pointing in the direction of stellar rotation. We scan all (projected) image pixels within a circle to get the  $T_i^4$  values for every  $x_i|y_i$  ( $i=1\dots n$ ) pair within the circle. The resulting sampling is set by the 100 dpi size of the movie images of the apparent disk. It yields an enclosing grid of about  $370 \times 370$  pixels in size, of which  $n=107521$  are within the circle. The coordinates of the photocenter are then given in Eq. (7) as

$$x_p = \frac{\sum_{i=1}^n T_i^4 x_i}{\sum_{i=1}^n T_i^4} \quad \text{and} \quad y_p = \frac{\sum_{i=1}^n T_i^4 y_i}{\sum_{i=1}^n T_i^4}, \quad (7)$$

and the radial offset  $r_p$  of the photocenter from  $0|0$  of the disk is given in Eq. (8)

$$r_p = \sqrt{x_p^2 + y_p^2}. \quad (8)$$

### Periods and errors

For the period determinations in this paper, we used the generalized Lomb Scargle (GLS) approach<sup>65</sup> and complemented it with phase dispersion minimization (PDM<sup>66</sup>). The Lomb-Scargle (LS) periodogram<sup>67,68</sup> as a variant of a Fourier transformation, is the least-squares fitting of a harmonic (sinusoidal) function to a time series. A seemingly model-free method like PDM can be seen as the least-squares fit of a piecewise constant function to the (phase-folded) data, rendering the PDM method similar to the analysis of  $\chi^2$  reduction in methods fitting data models. Frequencies were searched at an equidistant sampling starting at  $f_{\min} = 0.0001 \text{ c d}^{-1}$  and extending to  $f_{\max} = 1 \text{ c d}^{-1}$ , such that  $10^5$  frequencies were scanned.

From fitting a single harmonic with a particular period, one can read off formal errors from the covariance matrix of the fit. However, such formal errors crucially depend on a proper error estimation of the individual data point and cannot be trusted blindly. We obtain a more robust estimation with the following procedure. First, an artificial data set is created by letting the data, in our case  $T_{\text{eff}}$ , vary randomly around

the nominal value following a Gaussian distribution of a (prescribed) average error. Then we calculate the maximum of the LS peak at the period of interest. This is repeated  $\sim 10,000$  times and defines the error of the period as the standard deviation of the period distribution obtained. If we prescribe an error for  $T_{\text{eff}}$  of 26 K following Table 1, we obtain an error estimate for the 1514-d period of  $\pm 83$  d, that is, a 5% error. Doing the same for the rotational period, we obtain  $23.8016 \pm 0.003$  d, a 0.01% error, from  $T_{\text{eff}}$ . Redoing the same calculation with a hypothetical error for  $T_{\text{eff}}$  of 100 K per data point lets the long period vanish, while the rotation period is still retrieved at  $23.8 \pm 0.1$  d.

### Generation of the movie

A “movie” is a series of images at equidistant times. However, because our Doppler images were not taken strictly equidistant in time, variable gaps between consecutive Doppler maps exist, and an adaptation to the timeline was required. While time gaps during an observational season were rare and short (a few days at maximum), gaps from one observational season to the next spanned, on average, four months, or five stellar rotations, every year. We tackle this by computing interpolated images on a pixel-by-pixel level. The interpolation is always done linearly between the two nearest-in-time Doppler images and is computed every day at 12:00 UTC during the entire 16-year period. It results in altogether 5668 interpolated images equidistantly spaced in time, which are then used for the movies.

When making the fixed-frame movies (in our case the Aitoff, Mercator, and pole-on projections) the interpolated images can be thus just strung one after the other. However, when making the rotating-star movie (Supplementary Movies 6 and 7), the interpolated images were additionally rotated into the rotational phase defined by the images’ respective time.

Our interpolation strategy avoids artificial (seasonal) spot jumps from one image to the next by filling the time gap with a gradual change from the last image of the previous season to the first image of the next season. For the movie viewer, these seasonal time-gap fillers appear as a more-or-less standstill of the long-term star spot evolution. We emphasize that the interpolated images are not considered for any kind of scientific analysis and are only intended for proper visualization. This is also highlighted in the graphics of the full 16-year coverage of the spot-filling factor and surface flux (in Fig. 3) as well as of the photocenter (Fig. 4) by identifying the times with interpolated images.

### Data availability

The reduced spectroscopic and photometric data that support the findings of this study are available in Data Services AIP at [https://data.aip.de/projects/xx\\_tri.html](https://data.aip.de/projects/xx_tri.html) with the identifier doi:10.17876/data/2023\_2. Supplementary Data 1 and 2 are provided as separate files in ascii format. Secondary data generated in this study is provided in the file Source Data. It includes the data for Figs. 3a–c, 4b, and 5, and Supplementary Figs. 7b, 8, and 10. Gaia DR3 data were extracted from the Gaia archive <https://gaiaarchive.eu/gaia-data-release-3-dr3/>. VALD data were extracted from <http://vald.astro.uu.se/~vald/>. MARCS and ATLAS-9 model atmospheres were extracted from <https://marcs.astro.uu.se/> and the Kurucz CD-ROM from <https://wwwuser.oats.inaf.it/fiorella.castelli/grids.html>, respectively. The NASA/IPAC dust maps are available at <https://irsa.ipac.caltech.edu/applications/DUST/>. The ESA Hipparcos catalogs are available at <https://www.cosmos.esa.int/web/hipparcos/catalogues>. PARSEC 2.0 isochrones are available at <http://stev.oapd.inaf.it/PARSEC>. The datasets generated during and/or analyzed during the current study are available from the corresponding author upon request. Source data are provided with this paper.

### Code availability

The automatic SESDR data-reduction pipeline, the iMAP line-profile inversion software, the APOFIS isochrone fitting routine, and the

ParSES spectral-analysis package were described in the open-source literature and are under continuous development. They can be obtained from the authors via an e-mail request to K.G.S. Open-source software was Turbospectrum (<https://github.com/bertrandplez/Turbospectrum2019>) with line data from VALD, as well as ExoCTK (<https://exoctk.readthedocs.io/en/latest/>), Nightfall (<https://www.physik.uni-hamburg.de/en/hs/group--schmidt/team-members/wichmann-rainer/nightfall.html>), and PHOEBE (<https://www.phoebe-project.org/>). These codes/routines are publicly documented and can be requested from the respective authors as cited.

### References

- Solanki, S. K. Sunspots: an overview. *Astron. Astrophys. Rev.* **11**, 153 (2003).
- Strassmeier, K. G. Starspots. *Astron. Astrophys. Rev.* **17**, 251 (2009).
- Deutsch, A. J. Harmonic analysis of the periodic spectrum variables. In: Lehnert, B. et al. (eds.) *Electromagnetic Phenomena in Cosmical Physics*, vol. 6 of IAU Symposium, 209 (1958).
- Goncharski, A. Reconstruction of local line profiles from those observed in an Ap spectrum. *Sov. Astron. Lett.* **3**, 147 (1977).
- Vogt, S. S. & Penrod, G. D. Doppler imaging of spotted stars: application to the RS Canum Venaticorum star HR 1099. *Publ. Astron. Soc. Pac.* **95**, 565 (1983).
- Piskunov, N. E. & Rice, J. B. Techniques for surface imaging of stars. *Publ. Astron. Soc. Pac.* **105**, 1415 (1993).
- Kürster, M. Doppler imaging with a CLEAN-like approach. I. A newly developed algorithm, simulations and tests. *Astron. Astrophys.* **274**, 851 (1993).
- Rice, J. B. Doppler imaging of stellar surfaces. In: Strassmeier, K. G., & Linsky, J. L. (eds.) *Stellar Surface Structure*, vol. 176 of IAU Symposium, 19 (1990).
- Strassmeier, K. G. Doppler imaging of stellar surface structure XI. The super starspots on the K0 giant HD 12545: larger than the entire Sun. *Astron. Astrophys.* **347**, 225 (1999).
- Künstler, A., Carroll, T. A. & Strassmeier, K. G. Spot evolution on the red giant star XX Triangulum. A starspot-decay analysis based on time-series Doppler imaging. *Astron. Astrophys.* **578**, A101 (2015).
- Gaia, C. et al. Gaia data release 3. Summary of the contents and survey properties. *arXiv* <https://arxiv.org/abs/2208.00211> (2022).
- van Leeuwen, F. Validation of the new Hipparcos reduction. *Astron. Astrophys.* **474**, 653 (2007).
- ESA. The Hipparcos and Tycho Catalogues. *ESA SP 1200*, (1997).
- Schlafly, E. F. & Finkbeiner, D. P. Measuring reddening with sloan digital sky survey stellar spectra and recalibrating SFD. *Astrophys. J.* **737**, 103 (2011).
- Strassmeier, K. G., Carroll, T. A. & Ilyin, I. V. Warm and cool starspots with opposite polarities. A high-resolution Zeeman-Doppler-Imaging study of II Pegasi with PEPSI. *Astron. Astrophys.* **625**, A27 (2019).
- Strassmeier, K. G. & Rice, J. B. Doppler imaging of stellar surface structure. IX. A high-resolution image of the weak-lined T Tauri star HDE 283572 = V987 Tauri. *Astron. Astrophys.* **339**, 497 (1998).
- Shapiro, A. I., Solanki, S. K. & Krivova, N. A. Predictions of astrometric jitter for sun-like stars. I. The model and its application to the sun as seen from the ecliptic. *Astrophys. J.* **908**, 223 (2021).
- Sowmya, K. et al. Predictions of astrometric jitter for sun-like stars. II. Dependence on inclination, metallicity, and active-region nesting. *Astrophys. J.* **919**, 94 (2021).
- Oláh, K. et al. Magnitude-range brightness variations of overactive K giants. *Astron. Astrophys.* **572**, A94 (2014).
- Strassmeier, K. G. et al. The STELLA robotic observatory. *Astron. Nachr.* **325**, 527 (2004).
- Granzer, T. What makes an automated telescope robotic? *Astron. Nachr.* **325**, 513 (2004).



22. Strassmeier, K. G. et al. The STELLA robotic observatory on Tenerife. *Adv. Astron.* **2010**, ID970306 (2010).
23. Weber, M., Granzer, T., & Strassmeier, K. G. STELLA: 10 years of robotic observations on Tenerife. In: Peck, A. B., Seaman, R. L. & Benn, H. C. R. (eds.) *Observatory Operations: Strategies, Processes, and Systems VI*, vol. 9910 of *Society of Photo-Optical Instrumentation Engineers (SPIE) Conference Series*, 99100N (2016).
24. Strassmeier, K. G., Boyd, L. J., Epand, D. H. & Granzer, T. Wolfgang-Amadeus: the University of Vienna twin automatic photoelectric telescope. *Publ. Astron. Soc. Pac.* **109**, 697 (1997).
25. Carroll, T. A., Strassmeier, K. G., Rice, J. B. & Künstler, A. The magnetic field topology of the weak-lined T Tauri star V410 Tauri. New strategies for Zeeman-Doppler imaging. *Astron. Astrophys.* **548**, A95 (2012).
26. Vogt, S. S., Penrod, G. D. & Hatzes, A. P. Doppler images of rotating stars using maximum entropy image reconstruction. *Astrophys. J.* **321**, 496 (1987).
27. Meunier, N., Lagrange, A.-M., Boulet, T. & Borgniet, S. Activity time series of old stars from late F to early K. I. Simulating radial velocity, astrometry, photometry, and chromospheric emission. *Astron. Astrophys.* **627**, A56 (2019).
28. Morris, B. M. et al. Spotting stellar activity cycles in Gaia astrometry. *Mon. Not. R. Astron. Soc.* **476**, 5408 (2018).
29. do Nascimento, J. R. et al. A Hale-like cycle in the solar twin 18 Scorpii. *Astrophys. J.* **958**, 57 (2023).
30. Roettenbacher, R. M. et al. No Sun-like dynamo on the active star  $\zeta$  Andromedae from starspot asymmetry. *Nature* **533**, 217 (2016).
31. Roettenbacher, R. M. et al. Contemporaneous imaging comparisons of the spotted giant  $\sigma$  Geminorum using interferometric, spectroscopic, and photometric data. *Astrophys. J.* **849**, 120 (2017).
32. Brun, A. S. & Palacios, A. Numerical simulations of a rotating red giant star. I. Three-dimensional models of turbulent convection and associated mean flows. *Astrophys. J.* **702**, 1078 (2009).
33. Inceoglu, F., Simoniello, R., Arlt, R. & Rempel, M. Constraining non-linear dynamo models using quasi-biennial oscillations from sunspot area data. *Astron. Astrophys.* **625**, A117 (2019).
34. Charbonneau, P. Dynamo models of the solar cycle. *Living Rev. Sol. Phys.* **17**, 4 (2020).
35. Palacios, A. & Brun, A. S. On dynamo action in the giant star Pollux: first results. *IAU Symp.* **302**, 363 (2014).
36. Bartel, M. F. et al. VLBI for gravity probe B: the guide star, IM Pegasi. *Class. Quantum Grav.* **32**, 224021 (2015).
37. Marsden, S. C. et al. Starspots and relativity: applied Doppler imaging for the gravity probe B mission. *Astron. Nachr.* **328**, 1047 (2007).
38. Berdyugina, S. V., & Marsden, S. C. Applied doppler imaging: can magnetic activity of IM Pegasi affect the gravity probe B mission? In: Casini, R. & Lites, B. W. (eds.) *Solar Polarization 4*, vol. 358 of *ASP Conference Series*, 385 (2006).
39. Marsden, S. C. et al. A Sun in the spectroscopic binary IM Pegasi, the guide star for the Gravity Probe B mission. *Astrophys. J.* **634**, L173 (2005).
40. Perryman, M., Hartman, J., Bakos, G. A. & Lindegren, L. Astrometric exoplanet detection with GAIA. *Astrophys. J.* **797**, 14 (2014).
41. Rice, J. B., Wehlau, W. H. & Khokhlova, V. Mapping stellar surfaces by Doppler imaging: technique and application. *Astron. Astrophys.* **208**, 179 (1989).
42. Piskunov, N. E. Harmonic analysis of the periodic spectrum variables. In: Tuominen, I., Moss, D. & Rüdiger, G. (eds.) *The Sun and Cool Stars: Activity, Magnetism, Dynamos*, vol. 130 of *IAU Colloquium*, 309 (1990).
43. Brown, S., Donati, J.-F., Rees, D. & Semel, M. Zeeman-Doppler imaging of solar-type and AP stars. IV. Maximum entropy reconstruction of 2D magnetic topologies. *Astron. Astrophys.* **250**, 463 (1991).
44. Collier Cameron, A. Modelling stellar photospheric spots using spectroscopy. In: Byrne, P., & Mullan, D. (eds.) *Surface Inhomogeneities on Late-type Stars*, vol. 397 of *Lecture Notes in Physics*, 33 (1992).
45. Engl, H. W., Hanke, M., & Neubauer, A. Regularization of Inverse problems, mathematics and its application, (Dordrecht, The Netherlands: Kluwer Academic Publishers) (1996).
46. Carroll, T. A., Kopf, M. & Strassmeier, K. G. A fast method for Stokes profile synthesis. Radiative transfer modeling for ZDI and Stokes profile inversion. *Astron. Astrophys.* **488**, 781 (2008).
47. Ryabchikova, T. et al. A major upgrade of the VALD database. *Phys. Scr.* **90**, ID054005 (2015).
48. Kurucz, R. L. ATLAS9 Stellar atmosphere programs and 2 km/s grid. CD-ROM No 13. (1993).
49. Castelli, F. & Kurucz, R. L. New grids of ATLAS9 model atmospheres. *IAU Symp.* **210**, A20 (2003).
50. Strassmeier, K. G. et al. VPNEP: detailed characterization of TESS targets around the Northern Ecliptic pole. I. Survey design, pilot analysis, and initial data release. *Astron. Astrophys.* **671**, A7 (2023).
51. Bressan, A. et al. PARSEC: stellar tracks and isochrones with the PAdova and TRIeste stellar evolution code. *Mon. Not. R. Astron. Soc.* **427**, 127 (2012).
52. Kővári, Z. S. et al. Doppler imaging of stellar surface structure. XXIII. The ellipsoidal K giant binary zeta Andromedae. *Astron. Astrophys.* **463**, 1071 (2007).
53. Roettenbacher, R. M. et al. Detecting the companions and ellipsoidal variations of RS CVn primaries. I. Sigma Geminorum. *Astrophys. J.* **807**, 23 (2015).
54. Wichmann, R. Nightfall: animated views of eclipsing binary stars. Astrophysics Source Code Library, record ascl:1106.016 (2011).
55. Prsa, A., Matijevic, G., Latkovic, O., Vilardell, F., & Wils, P. PHOEBE: physics of eclipsing binaries. Astrophysics Source Code Library, record ascl:1106.002 (2011).
56. Allende-Prieto, C. Automated analysis of stellar spectra. *Astron. Nachr.* **325**, 604 (2004).
57. Gustafsson, B. et al. A grid of MARCS model atmospheres for late-type stars. I. Methods and general properties. *Astron. Astrophys.* **486**, 951 (2008).
58. Plez, B. Turbospectrum. Astrophysics Source Code Library, record ascl:1205.004. (2012).
59. Allende-Prieto, C. et al. A spectroscopic study of the ancient Milky Way: F- and G-type stars in the third data release of the Sloan digital sky survey. *Astrophys. J.* **636**, 804 (2006).
60. Jofré, P. et al. Gaia FGK benchmark stars: metallicity. *Astron. Astrophys.* **564**, A133 (2014).
61. Rice, J. B. & Strassmeier, K. G. Doppler imaging from artificial data. Testing the temperature inversion from spectral-line profiles. *Astron. Astrophys. Suppl.* **147**, 151 (2000).
62. Strassmeier, K. G. et al. Spatially resolving the accretion shocks on the rapidly-rotating M0 T-Tauri star MN Lupi. *Astron. Astrophys.* **440**, 1105 (2005).
63. ExoCTK consortium JWST Exoplanet Characterization Toolkit (ExoCTK). v1.2.4: <https://exoctk.stsci.edu/>. (2022).
64. Kreidberg, L. batman: Basic transit model cAlculationN in Python. *Publ. Astron. Soc. Pac.* **127**, 1161 (2015).
65. Zechmeister, M. & Kürster, M. The generalised Lomb-Scargle periodogram. A new formalism for the floating-mean and Keplerian periodograms. *Astron. Astrophys.* **496**, 577 (2009).
66. Stellingwerf, R. F. Period determination using phase dispersion minimization. *Astrophys. J.* **224**, 953 (1978).
67. Lomb, N. R. Least-squares frequency analysis of unequally spaced data. *Ap. Space Sci.* **39**, 447 (1976).
68. Scargle, J. D. Studies in astronomical time series analysis. II. Statistical aspects of spectral analysis of unevenly spaced data. *Astrophys. J.* **263**, 835 (1982).



## Acknowledgements

K.G.S. acknowledges the institutional support for STELLA from the state Ministry of Science, research, and Culture (MWFK) of Brandenburg as well as from the German Federal Ministry of Education and Research (BMBF). Zs.K. was supported by the Hungarian National Research Development and Innovation Office grants OTKA K-131508 and KKP-143986. We thank our colleagues Arto Järvinen and Jörg Weingrill for keeping STELLA running, and also the AIP technical support staff, in particular the late Emil Popow, but also Manfred Woche, Jens Paschke, Svend-Marian Bauer, Thomas Fechner, Frank Dionies, Wilbert Bittner, and Hakan Önel. Thorsten Carroll is thanked for providing the latest version of the *i*MAP software, Rainer Arlt for discussions on giant-star dynamos, Katalin Oláh for her photometric help, and Bálint Seli, Ádám Radványi, and Levente Kriskovics for helping out with software issues. Our colleagues at the Centre for Data Science and Digital Development at the Budapest-based Moholy-Nagy University of Art and Design (MOME), are thanked for providing the movies. All institutions of the author affiliations obey their federal Inclusion & Ethics standards. Based on data obtained with the STELLA robotic telescopes in Tenerife, Spain, an AIP facility jointly operated by AIP and IAC at the Observatorio del Teide of the Instituto de Astrofísica de Canarias (IAC).

## Author contributions

K.G.S. wrote the main text and supplementary info of the manuscript, defined the target and its observations, is the P.I. of STELLA and the APTs, and supervised the Doppler imaging procedure. Zs.K. performed the Doppler imaging and the image photocenter computations and supervised the movie makers. M.W. carried out the SES data reduction and ran SES and the ParSES synthesis code. T.G. operated STELLA and the APTs and searched for periods in his spare time. All authors were involved in the review of the results and the comments on the manuscript.

## Competing interests

The authors declare no competing interests.

## Additional information

**Supplementary information** The online version contains supplementary material available at <https://doi.org/10.1038/s41467-024-54329-4>.

**Correspondence** and requests for materials should be addressed to K. G. Strassmeier.

**Peer review information** *Nature Communications* thanks the anonymous reviewers for their contribution to the peer review of this work. A peer review file is available.

**Reprints and permissions information** is available at <http://www.nature.com/reprints>

**Publisher's note** Springer Nature remains neutral with regard to jurisdictional claims in published maps and institutional affiliations.

**Open Access** This article is licensed under a Creative Commons Attribution-NonCommercial-NoDerivatives 4.0 International License, which permits any non-commercial use, sharing, distribution and reproduction in any medium or format, as long as you give appropriate credit to the original author(s) and the source, provide a link to the Creative Commons licence, and indicate if you modified the licensed material. You do not have permission under this licence to share adapted material derived from this article or parts of it. The images or other third party material in this article are included in the article's Creative Commons licence, unless indicated otherwise in a credit line to the material. If material is not included in the article's Creative Commons licence and your intended use is not permitted by statutory regulation or exceeds the permitted use, you will need to obtain permission directly from the copyright holder. To view a copy of this licence, visit <http://creativecommons.org/licenses/by-nc-nd/4.0/>.

© The Author(s) 2024